Procedures for offline grid nesting in regional ocean models

Evan Mason [a,*], Jeroen Molemaker [b,**], Alexander F. Shchepetkin [b], Francois Colas [b], James C. McWilliams [b], Pablo Sangrà [a]

[a] *Facultad de Ciencias del Mar, Universidad de Las Palmas de Gran Canaria, 35017, Las Palmas de Gran Canaria, Spain*
[b] *Institute of Geophysics and Planetary Physics, University of California Los Angeles, Los Angeles, California, USA*

ABSTRACT

One-way offline nesting of a primitive-equation regional ocean numerical model (ROMS) is investigated, with special attention to the boundary forcing file creation process. The model has a modified open boundary condition which minimises false wave reflections, and is optimised to utilise high-frequency boundary updates. The model configuration features a previously computed solution which supplies boundary forcing data to an interior domain with an increased grid resolution. At the open boundaries of the interior grid (the child) the topography is matched to that of the outer grid (the parent), over a narrow transition region. A correction is applied to the normal baroclinic and barotropic velocities at the open boundaries of the child to ensure volume conservation. It is shown that these steps, together with a carefully constructed interpolation of the parent data, lead to a high-quality child solution, with minimal artifacts such as persistent *rim currents* and wave reflections at the boundaries.

Sensitivity experiments provide information about the robustness of the model open boundary condition to perturbations in the surface wind stress forcing field, to the perturbation of the volume conservation enforcement in the boundary forcing, and to perturbation of the vertical density structure in the boundary forcing. This knowledge is important when extending the nesting technique to include external data from alien sources, such as ocean models with physics and/or numerics different from ROMS, or from observed climatologies of temperature, salinity and sea level.

© 2010 Elsevier Ltd. All rights reserved.

1. Introduction

In numerical oceanic and atmospheric modelling, downscaling is a practical solution to the problem of resolving wide-ranging spatial and temporal scales of motion under the constraint of finite computing power and storage (e.g., Beckers et al., 1997; Penven et al., 2006; Auclair et al., 2006; Cailleau et al., 2008). Downscaling involves the embedding, or nesting, of multiple model grids one within the other, each successive grid having a higher resolution than its parent. Such grid configurations may be run independently (offline nesting) or synchronously (online nesting). The important distinction between the two is the frequency of the boundary updates, which is higher for the online case. Higher frequencies are desirable but, in the offline case, judicious choice of the updating interval allows the resolution of the primary features of interest. Both approaches therefore yield realistic high-resolution solutions permitting study of local problems: the large-scale mean circulation and its associated variability (mostly mesoscale, plus seasonal

and possibly inter-annual contributions) is provided by and passed down from the outermost parent, while the innermost child generates the high-resolution mesoscale and submesoscale data for the physical problem at hand.

Downscaling is a one-way process, in that information is passed solely downstream, from parent to child. Upscaling is the reverse process, where information is passed from a child solution back up to the parent. Two-way nesting brings together downscaling and upscaling, so that there is a dual exchange of information: parent-to-child and child-to-parent. This technique is necessarily online, requiring additional software tools beyond the model code itself to facilitate the information exchange.

In regional oceanic modelling, the AGRIF Fortran (Adaptive Grid Refinement in Fortran; Debreu et al., 2008) package is one such tool in use. AGRIF has been incorporated into, amongst others, the ROMS (Regional Ocean Modelling System; Shchepetkin and McWilliams, 2005; Shchepetkin and McWilliams, 2009) and NEMO-OPA (Madec, 2008) hydrodynamic models, permitting synchronous multi-level downscaled simulations. An evaluation of the system is presented by Penven et al. (2006), who conducted nested ROMS experiments for the US West Coast. Cailleau et al. (2008), in a comparative study of different nesting techniques, report the use of two-way OPA nesting using AGRIF. These authors also introduce

* Corresponding author. Tel.: +349 3 230 9602.
** Corresponding author.
E-mail addresses: emason@icm.csic.es (E. Mason), nmolem@atmos.ucla.edu (J. Molemaker).

a more sophisticated coupling method, the *Schwarz* domain decomposition method, which is shown to improve on the two-way solution, albeit at a high computational cost. A recent development is a ROMS-AGRIF two-way setup, described by Debreu (2008). See Debreu and Blayo (2008) for a review of the algorithms used in two-way embedding.

Several papers that are focused on regional operational oceanography such as Onken et al. (2005), Leslie et al. (2008) and Lam et al. (2009), report the use of nesting techniques by means of the Harvard Ocean Prediction System (HOPS; Robinson, 1999). While the approach within HOPS appears to be similar to the one described here, it is difficult to judge since the discrete algorithms that are implemented in HOPS do not appear to be well documented in the literature. One documented difference is that HOPS employs an open boundary condition for barotropic transport that is one suggested by Charney et al. (1950). Another aspect that makes it challenging to directly compare our current approach with that of the papers above is that they mostly conduct simulations of short duration while we focus on boundary artifacts that may arise during long-term simulations. In Onken et al. (2005) a degradation of the interior solution is reported for longer runs. Also, the use of data assimilation in operational oceanography makes it difficult to cleanly assess the effect of nesting procedures. In another approach to regional operational modelling (Estournel et al., 2009), a Flather condition is used for the barotropic component of the velocities, while a radiative condition with a fixed phase speed is used for the baroclinic component.

The purpose of this paper is to show how careful formulations of one-way offline nesting are still valuable in regional ocean modelling, despite the emergence of more advanced two-way methods. Offline nesting permits great flexibility in terms of grid dimensions and orientation. Grids may be rotated, enabling boundaries to be aligned with coastlines to maximise the oceanic extent of the computational domain. Furthermore, time step and grid resolution ratios between each grid and its parent may be varied. Downscaling is often sufficient to provide an adequate physical posing of a problem, so that two-way nesting becomes excessively laborious. In this respect, there is still no clear idea of when one approach or the other may be expected to make an important difference.

1.1. 2D versus 3D boundary forcing methods

ROMS permits the use of either 2D or 3D boundary forcing. 3D boundary forcing is the common practice in many ocean models, where the parent 3D variables (i.e., baroclinic velocities and tracers) used at the child boundaries are stored in three-dimensional arrays on the child-grid. 2D variables (barotropic velocities and sea surface height) are stored in two-dimensional arrays. The bulk of these data, i.e., those within the interior of the domain, are redundant because only data at the boundary itself, plus a several-grid-cell-deep variable-strength relaxation (or *nudging*) layer, are used. Within the volumetric nudging layer the model variables are restored towards the 3D boundary forcing values (Marchesiello et al., 2001). In practical terms, this has restricted regional ocean modellers with regards to the size of child domains and, more importantly, the temporal frequency of the boundary forcing. Without these restrictions the storage size of 3D boundary forcing files becomes prohibitive, making it difficult to provide boundary information which resolves the mesoscale, let alone the submesoscale. Predictive modellers do not face these restrictions because of the *a priori* short time scales of such simulations.

The use of 2D boundary forcing files, where only information at the boundaries is used (i.e., no interior nudging layer), is clearly more efficient in terms of disc storage than 3D. Using this approach together with adequate computing resources, combinations of long solutions (multiple model years, see for example, Section 4) on

large grids (order of $1000 \times 1000 \times 80$ grid-points; e.g., Capet et al., 2008b; McWilliams et al., 2009) with high-resolution (in time, <1 day, and space, <100 m) boundary inputs, are feasible. However, to fully profit from the use of high-frequency boundary input, it has been necessary to modify the ROMS barotropic velocity Open Boundary Condition (OBC), and switch to an upwind advection scheme for tracers at the open boundary. More details are given in Section 2.

1.2. Rim currents

The volumetric nudging used in the 3D boundary forcing method is not possible with the 2D method; here we choose not to explore any sensitivity to the loss of this option. However, nudging is often credited with reducing so-called *rim currents*, which are a primary error mode that may occur in ocean model simulations. Fig. 1 shows an example of a persistent rim current: In the v-component of the annual mean velocity from a 50-year ROMS simulation of the northeast Atlantic Ocean at 7.5 km resolution (Mason, 2009), a narrow strip of anomalous velocities (positive and negative) is seen along the western boundary.

Rim currents are a result of mismatches between the boundary forcing and the evolving child solution, and also the ability of the chosen OBC to ameliorate mismatches. Mismatches may occur in the stratification, particularly within the mixed layer; they may also arise if there are differences in the parent and child surface forcings, switching from one wind product to another for example; and also if volume conservation is not enforced in the boundary velocities. Rim currents, if present, show up most readily by viewing just the tangential component of the velocity along a boundary as in Fig. 1. However, because we have largely minimised rim currents in our ROMS-to-ROMS nested solutions, in the following sections we shall show them using relative vorticity, which is especially sensitive to velocity anomalies.

We have developed a methodology to facilitate downscaling within a ROMS framework. In the following sections we present results from a ROMS configuration centred on the Canary Island archipelago in the northeast Atlantic, prepared using the new methodology. In Section 2 we briefly describe the ROMS model that provides the numerical framework for our experiments and the regional configuration that we have designed, and we also introduce the downscaling techniques that have been developed for the experiments. Results are presented in Section 3, which demonstrate the effectiveness of the procedures we use. In Section 4 we test the model's sensitivity to perturbations in the boundary and surface forcing data. Section 5 concludes with a discussion of the implications of our results.

2. Numerical methods and configuration

2.1. The ROMS model

ROMS is a primitive-equation, free-surface model which uses an orthogonal curvilinear coordinate system in the horizontal direction and a generalised terrain-following coordinate in the vertical. For the purpose of computational efficiency the code utilises the natural time scale separation of barotropic and baroclinic processes by employing a mode-splitting algorithm which solves the vertically-integrated barotropic momentum equations using a much smaller time step. A specially designed fast-time-averaging procedure prevents aliasing of processes unresolved by the longer baroclinic time step and, at the same time, maintains all necessary conservation properties (Shchepetkin and McWilliams, 2005). For this study we use the UCLA variant of the ROMS kernel (Shchepetkin and McWilliams, 2009).
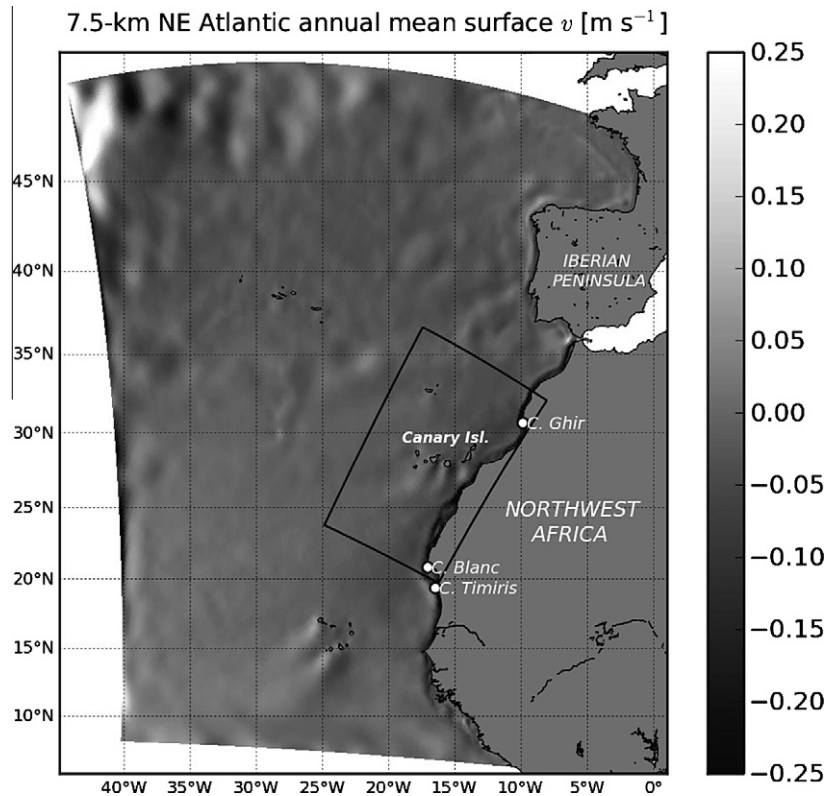
Fig. 1. Example of western boundary rim currents in the v-component of the mean annual model velocity of the 7.5 km parent (L0) solution, which covers the northeast Atlantic. Black lines demark the boundary of the child (L1) domain discussed throughout the present text. The locations of the Canary Islands and capes mentioned in the text are marked. Note that the strong positive velocity in the northwest corner is likely to be a realistic feature.

From the very beginning ROMS was intended to be a regional model, which means that a numerical side-boundary forcing algorithm must be developed to supply external data at the open boundary of a limited-area domain.

2.1.1. Overview of numerical boundary condition algorithms

The task of the OBC is to supply the external information needed by the limited-area model domain at the boundaries, whilst, at the same time, allowing information generated within the model domain to exit through the boundaries with minimal artificial influence onto the interior solution. The problem is mathematically non-trivial, because it is impossible to predict *a priori* which boundaries play the role of inflow or outflow and, furthermore, the same segment of open boundary may be both inflowing and outflowing for different physical processes. Also, because of the mode-splitting used by the main time stepping algorithm of ROMS, the boundary conditions must be formulated in terms of model variables, i.e., separately for the barotropic and baroclinic modes. In the approach we choose, the external data are provided along single rows at the open boundaries, i.e., there is no volumetric nudging over an interior boundary layer; for this approach to be successful, the performance of the OBC and the quality of the external data are critical. Lateral viscosity and diffusion are, however, allowed to decrease away from the boundary within a so-called *sponge* layer, in order to smooth minor inconsistencies between the evolving model solution and the external data. The values and profiles of viscosity and diffusivity within the sponge layers must be prescribed.

For the barotropic mode, the free surface and normal velocity components utilise a Flather-type condition (Flather, 1976), which is based on radiation and the prescription of *characteristic variables* (Riemann invariants; Blayo and Debreu, 2005). This new numerical implementation warrants a more detailed description which we

provide below. For the tangential velocity, an upstream advection scheme is used for both outflow and inflow. This uses a fully 2D *corner algorithm* involving all nearest points. The local advection velocity is used for the phase speed. In the case of inflow, external data provided by a boundary file are used for the upstream donor-cell values. For outflow, the external data are ignored. There are no user-definable variable parameters (i.e., nudging time scales) associated with the barotropic mode boundary condition.

The baroclinic mode utilises, for the normal velocity components of the momentum equations, an Orlanski-type (Orlanski, 1976) condition with adaptive strong (weak) nudging for inflow (outflow). Parameters for the nudging strength must be defined by the user. For the tangential velocity an upstream advection scheme with local advection velocity as phase speed is used. In the case of inflow, the external data are used for the upstream donor-cell value. For outflow, the external data are ignored. There are no tunable parameters to be defined. Tracers use an upstream advection scheme similar to that for the tangential velocity above. Again, no tunable parameters are involved.

2.1.2. Flather boundary conditions for staggered grids

The original rationale for the Flather boundary condition comes from the assumption that the dominant physical processes are surface gravity waves and the desire to allow incoming surface gravity waves specified by the external data to enter the computational domain, while at the same time achieving unimpeded radiation for the outgoing waves (Chapman, 1985). In practice this situation occurs only in purely tidal simulations in a small domain (hence it is physically acceptable to assume that the sea surface field is controlled entirely by the lateral boundaries while neglecting the effect of the gravitational tidal potential). Furthermore, ROMS, as a split-explicit model, averages barotropic processes over one baroclinic time step, effectively filtering out unresolved barotropic time scales, while the

slower barotropic processes (e.g., tides) behave as if the internal solution had adjusted itself instantaneously (from the point of view of the 3D mode, which resolves only time scales larger than the baroclinic time step, Δt) to the externally imposed boundary conditions. Thus, the ultimate goal of the Flather condition is to achieve the best possible matching between the model field with the external data for free surface elevation and barotropic (vertically-integrated) normal velocity component in situations when straightforward clamping of both would result in over-specification while, if taken alone, neither primitive variable can be used to specify a well-posed boundary problem. In contrast with the purely wave and tidal cases, posing of the problem in a regional configuration requires the specification of large-scale flow across the open boundaries. Previously in the case of rigid-lid models the barotropic component was simply prescribed by imposing Dirichlet-type boundary conditions on the barotropic streamfunction (Barnier et al., 1998; Marchesiello et al., 1998; de Miranda et al., 1999). This is possible because the free surface wave motions are excluded completely, while the remaining barotropic dynamics are governed by elliptic-type equations, which need all-round specified boundary conditions for mathematical well-posedness. Physically this means the specification of an external flow which is subject to the constraint of zero net flux for volume conservation.

In the case of a long-term, limited-area simulation using a free surface model the goal is essentially the same: to constrain the model solution to be close to the externally defined flow at the boundaries. However, the method of achieving it is different: it is no longer possible to simply impose the normal velocities as a hard constraint. There are two reasons for this: (i) doing so would not guarantee the proper integral value of the net flux, resulting in drift of horizontally-averaged free surface elevations and (ii) the appearance of a barotropic non-damped wave field trapped inside the model domain (recall that advective velocities are usually small in comparison with the external gravity wave speed, so prescribed boundaries would effectively behave as perfectly reflective rigid walls). To address both of these issues, Marchesiello et al. (2001) proposed a combination of an Orlanski-type radiation boundary condition applied to each prognostic boundary individually along with differential relaxation towards external data (with empirically chosen time scales; overall this can be classified as a soft constraint), and an integral flux constraint to avoid net volume gain or loss. A similar approach, except that a radiation boundary algorithm is applied to the difference between the model solution and external data, was explored by Perkins et al. (1997). Although both are viable approaches, in practice, success or failure depends on careful choice of user-defined parameters, often requiring elaborate empirical tuning to avoid artifacts associated with open boundaries. We are therefore motivated to explore an alternative approach which does not require such tuning.

The Flather-type characteristic boundary conditions are derived as follows:

$$\partial_t u = -g \cdot \partial_x \zeta, \quad \partial_t \zeta = -h \cdot \partial_x u, \tag{1}$$

with the possibility to rewrite the above in terms of characteristic variables:

$$\mathfrak{R}^{\pm} = u \pm \sqrt{\frac{g}{h}} \cdot \zeta, \quad \text{hence} \begin{cases} \partial_t \mathfrak{R}^+ + c \cdot \partial_x \mathfrak{R}^+ = 0, \\ \partial_t \mathfrak{R}^- - c \cdot \partial_x \mathfrak{R}^- = 0, \end{cases} \quad c = \sqrt{gh}, \tag{2}$$

so that $\mathfrak{R}^+$ and $\mathfrak{R}^-$ propagate to the right and to the left independently of each other with a known phase speed, c. This means that $\mathfrak{R}^- = \mathfrak{R}_0^-(x + ct) = const$ and $\mathfrak{R}^+ = \mathfrak{R}_0^+(x - ct) = const$ along their respective characteristics, $x \pm ct = const$. The boundary conditions for $\mathfrak{R}^+$ and $\mathfrak{R}^-$ are as follows: one must specify a value at the incoming side, while there is no need for a boundary condition at the outgoing side, hence:

$$\begin{array}{ll} \text{Left side}: & \text{Right side}: \\ \mathfrak{R}^+ = u^{(\text{ext})} + \sqrt{\frac{g}{h}} \cdot \zeta^{(\text{ext})}, & \mathfrak{R}^+ \text{ from free radiation condition}, \\ \mathfrak{R}^- \text{ from free radiation condition}, & \mathfrak{R}^- = u^{(\text{ext})} - \sqrt{\frac{g}{h}} \cdot \zeta^{(\text{ext})}, \end{array} \tag{3}$$

after which $\mathfrak{R}^+$ and $\mathfrak{R}^-$ are transformed back to the original variables u, ζ. In principle, Eq. (3) provides a method of solution for (1) not only near the boundaries, but also within the domain: one can discretise the latter using a non-staggered grid with u, ζ co-located; point-wise transform them into (2); and then solve as two independent advection problems for $\mathfrak{R}^+$, $\mathfrak{R}^-$. This approach is known as the Riemann solver for systems of equations such as, in the simplest cases, (1), and they are widely used for gas dynamical simulations, especially for shocks.

However, the majority of ocean models use horizontally-staggered grids, where cells for the free surface and velocity components are not co-located, and time step (1) directly using the original variables. This, however, cannot be applied to the boundaries, where the problem is well-posed only for $\mathfrak{R}^+$, $\mathfrak{R}^-$; but, at the same time, translation from u, ζ to $\mathfrak{R}^+$, $\mathfrak{R}^-$ is obscured because of the different locations of the variables. Nevertheless, the ocean modelling literature has numerous examples of the use of Flather boundary conditions, especially in the context of tidal simulations. In virtually all cases the dilemma of placing u, ζ at different locations has been addressed by applying an *ad hoc* interpolation scheme to translate each variable to the location of the other; see e.g., Chapman (1985) for a review. This procedure has several drawbacks, such as excessive reflections and the imposition of an additional restriction on time step size relative to the stability limit of the main scheme. Below we describe a numerical algorithm for Flather boundary conditions which is suitable for the staggered C-grid.

Assuming that the ghost-points of the free surface elevation, ζ, are located a half-grid-interval away from the normal velocity points, u, the purpose of the algorithm is to impose the normal velocity in such a way that Eq. (3) is respected. This translates into the following four steps:

- Radiate out (details are below) u, ζ independently from each other to a common location at each new time step:

$$\nearrow u^* = \tilde{u}_{j+\frac{1}{2}}^{n+1}, \qquad \nearrow \zeta^* = \tilde{\zeta}_{j+\frac{1}{2}}^{n+1}.$$

- Construct the outgoing characteristic variable, $\mathfrak{R}^+$ or $\mathfrak{R}^-$ depending on the side, using u^*, ζ^*, e.g., on the right-side boundary it is:

$$\mathfrak{R}^+ = u^* + \sqrt{\frac{g}{h}} \cdot \zeta^*,$$

where g is gravity and h is depth.
- Prescribe the incoming characteristic variable from external data, e.g., on the right-side:

$$\mathfrak{R}^- = (\mathfrak{R}^-)^{(\text{ext})} = u^{(\text{ext})} - \sqrt{\frac{g}{h}} \cdot \zeta^{(\text{ext})}.$$

- Translate back:

$$u_{j+\frac{1}{2}}^{n+1} = \frac{\mathfrak{R}^+ + \mathfrak{R}^-}{2} = \frac{u^* + u^{(\text{ext})}}{2} + \sqrt{\frac{g}{h}} \cdot \frac{\zeta^* - \zeta^{(\text{ext})}}{2}.$$

The above differs from the original Flather condition, $u = u^{(\text{ext})} + \sqrt{\frac{g}{h}}(\zeta^* - \zeta^{(\text{ext})})$. Overall, apart from the *radiate out* step, the above algorithm follows the characteristic method of Blayo and Debreu (2005). Note that $\mathfrak{R}^+$ and $\mathfrak{R}^-$ never appear explicitly in the code. Boundary conditions for ζ (i.e., setting ζ at ghost-points at a half-grid point outside the boundary row of u-points) are needed only by the radiation scheme; they are not needed outside of the Flather OBC and are therefore auxiliary. Since the time step
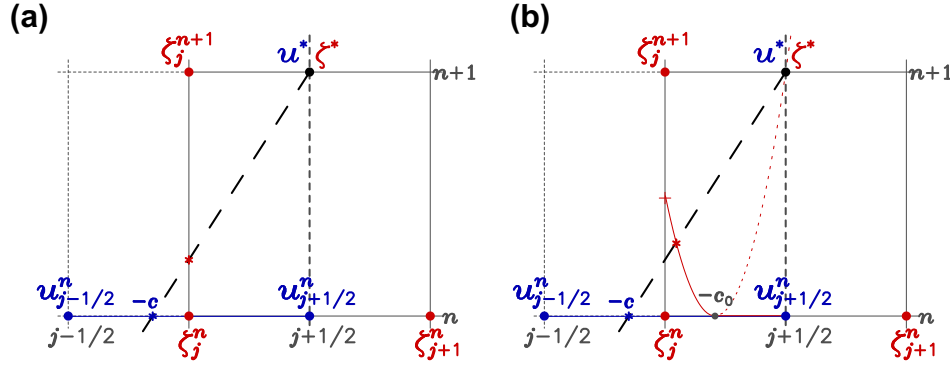
Fig. 2. Geometric explanation of computing ζ^* and u^* in Eqs. (4), (5) and (7). The open boundary is represented by the vertical dashed-line going through the normal velocity point $u_{j+\frac{1}{2}}$, so that the interior of the domain is to the left of it. The inclined line passing through ζ^* and u^* represents characteristic for the outbound Riemann invariant $\mathfrak{R}^+$. Since the time step is expected to be limited by the stability criterion $\tilde{c} < 1$, u^* can always be computed by an explicit scheme via (4). This is not the case for ζ^* because of its placement: Eq. (5) uses one of the two pairs of points, either ζ_j^n, ζ_{j+1}^n or ζ_j^n, ζ_j^{n+1}, depending on which segment is crossed by the characteristic (denoted by the red dot on the left panel). If $\tilde{c} = \frac{1}{2}$, then $\zeta^* = \zeta_j^n$, which results in a slow-growing instability due to the non-dissipative nature of the interpolation in this case. The right panel illustrates how to avoid using a single-point if $\tilde{c} = \frac{1}{2}$ by taking the value of ζ^* from the point where the characteristic intersects the parabolic of the segment starting at $-c^*$. (For interpretation of the references to colours in this figure caption the reader is referred to the web version of this article.)

Δt for the barotropic mode is always expected to be limited by the stability criterion for the explicit time stepping, a simple explicit radiation scheme is sufficient to compute u^*:

$$u^* = u_{j+\frac{1}{2}}^{n+1} = (1 - \tilde{c})u_{j+\frac{1}{2}}^n + \tilde{c}u_{j-\frac{1}{2}}^n, \tag{4}$$

without causing any additional time step restriction. In the above, $\tilde{c}$ is the normalised phase speed, i.e., the *Courant* number, $\tilde{c} = \Delta t \cdot c/\Delta x = \Delta t\sqrt{gh}/\Delta x < 1$.

For the free surface, ζ, the situation is more complicated because it is located half-way between u-points, and an explicit scheme would be stable only until $\tilde{c} \leqslant \frac{1}{2}$. One can devise a switched explicit–implicit scheme:

$$\zeta^* = \tilde{\zeta}_{j+\frac{1}{2}}^{n+1} = \begin{cases} \zeta_j^n\left(\frac{1}{2} + \tilde{c}\right) + \zeta_{j+1}^n\left(\frac{1}{2} - \tilde{c}\right), & \text{if } \tilde{c} < \frac{1}{2}, \\ \frac{\zeta_j^n + \zeta_j^{n+1}(2\tilde{c}-1)}{2\tilde{c}}, & \text{if } \tilde{c} > \frac{1}{2}, \end{cases} \tag{5}$$

which in its turn may need boundary values for the free surface at their natural location, ζ_{j+1}^n. These are computed using an auxiliary radiation boundary condition:

$$\zeta_j^{n+1} = (1 - \tilde{c})\zeta_{j+1}^n + \tilde{c}\zeta_j^n. \tag{6}$$

The sketch in Fig. 2a illustrates the placement of all variables.

Unfortunately the above algorithm suffers from a numerical instability when $\tilde{c} \approx \frac{1}{2}$. This instability is rather unusual because it occurs only within a narrow band of Courant numbers, and is associated with the fact that, if $\tilde{c} = \frac{1}{2}$, the outcome of the algorithm above is $\zeta^* = \zeta_j^n$ without any interpolation, and therefore dissipation. This instability can be eliminated by avoiding single-point values when $\tilde{c} = \frac{1}{2}$. To do so, we modify the algorithm as follows:

$$\zeta^* = \begin{cases} \zeta_j^n\left(\frac{1}{2} + \tilde{c}\right) + \zeta_{j+1}^n\left(\frac{1}{2} - \tilde{c}\right), & \text{if } \tilde{c} < \tilde{c}_0, \\ \zeta_j^n\left[\frac{1}{2} + \tilde{c}_0\left(2 - \frac{\tilde{c}_0}{\tilde{c}}\right) - \left(1 - \frac{\tilde{c}_0}{\tilde{c}}\right)^2\right] \\ \quad + \zeta_{j+1}^n\left[\frac{1}{2} - \tilde{c}_0\left(2 - \frac{\tilde{c}_0}{\tilde{c}}\right)\right] & , \quad \text{if } \tilde{c} > \tilde{c}_0, \\ \quad + \zeta_j^{n+1}\left(1 - \frac{\tilde{c}_0}{\tilde{c}}\right)^2 \end{cases} \tag{7}$$

where $\tilde{c}_0 = 1/(2 + \sqrt{2})$. This scheme, shown in Fig. 2(b), is always stable.[1]

---

[1] The *hole* instability, $\sim 0.48 < c < \sim 0.52$, was first encountered by Xavier Capet in a problem with realistic topography. It manifests itself as a blow-up at the boundary with the particular place dependent on the setting of the time step; no blow-up occurs for $\tilde{c} < \frac{1}{2}$. Because $\tilde{c}$ depends on the topography, and topography varies from very shallow near the coast to deep offshore, once the time step is large enough there is always a location at the boundary where $\tilde{c} \approx \frac{1}{2}$, resulting in instability. We are able now to reproduce it within an idealised wave problem.

The modified Flather OBC is applied for a simple test case (Fig. 3) to illustrate its effectiveness. In a simple square computational domain with a flat bottom, a solution is initialized with a radially symmetric barotropic wave. The wave radiates outwards towards the open boundaries from the centre. The signal reflected at the boundaries has an amplitude of just 1% of that of the original without the occurence of boundary trapped phenomena.

2.2. The ROMS configuration

The experiments are based on a regional model configuration of the Canary Basin in the subtropical northeast Atlantic Ocean. Fig. 4(a) shows the child grid (hereafter L1) topography, embedded within that of the parent grid (hereafter L0). The L1 domain includes the Canary Island archipelago that lies within the path of the equatorward-flowing Canary Current (CanC). A large portion of the Canary upwelling region is captured, from Cape Blanc (20.80°N) to Cape Ghir (30.65°N). In general, it may be expected that the direction of flow at the open boundaries will correspond to the local characteristics of the subtropical gyre (e.g., Hernández-Guerra et al., 2005; Machín et al., 2006). Hence, at the northern boundary inflow is expected to predominate and, at the south, outflow, both related to the CanC. At the western boundary, an inflow in the north is associated with the eastward-flowing Azores Current (AzC), while a weaker outflow to the south is due to an offshore branch of the CanC. Downstream of the Canary Islands, high mesoscale variability in the form of island-generated cyclonic and anticyclonic eddies is prevalent (e.g., Tejera et al., 2002; Sangrà et al., 2005). Filaments associated with the coastal upwelling interact with these eddies (e.g., Arístegui et al., 1994; Sandulescu et al., 2006).

The L1 grid has 332×534 grid-points, making physical dimensions of 996×1602 km². The horizontal resolution is $\Delta x = 3$ km. The domain is rotated clockwise 28.5°, so that the closed eastern boundary is aligned with the African coast. The southern, western and northern boundaries are open.

The parent L0 is an extensive domain that includes the entire Canary Basin (Fig. 1), extending between $\sim 12 - 45°N$ and 5–40°W. L0 has horizontal resolution $\Delta x = 7.5$ km. This implies a relatively small grid refinement coefficient between L0 and L1 of 2.5 (e.g., Debreu and Blayo, 2008). More about the preparation of L0 may be found in Mason (2009).

L0 and L1 both contain 32 vertical sigma-levels, with $hc = 120$ m and a surface stretching factor of $\theta_s = 6$ maintaining high vertical resolution throughout the surface layers (i.e., boundary layers) of
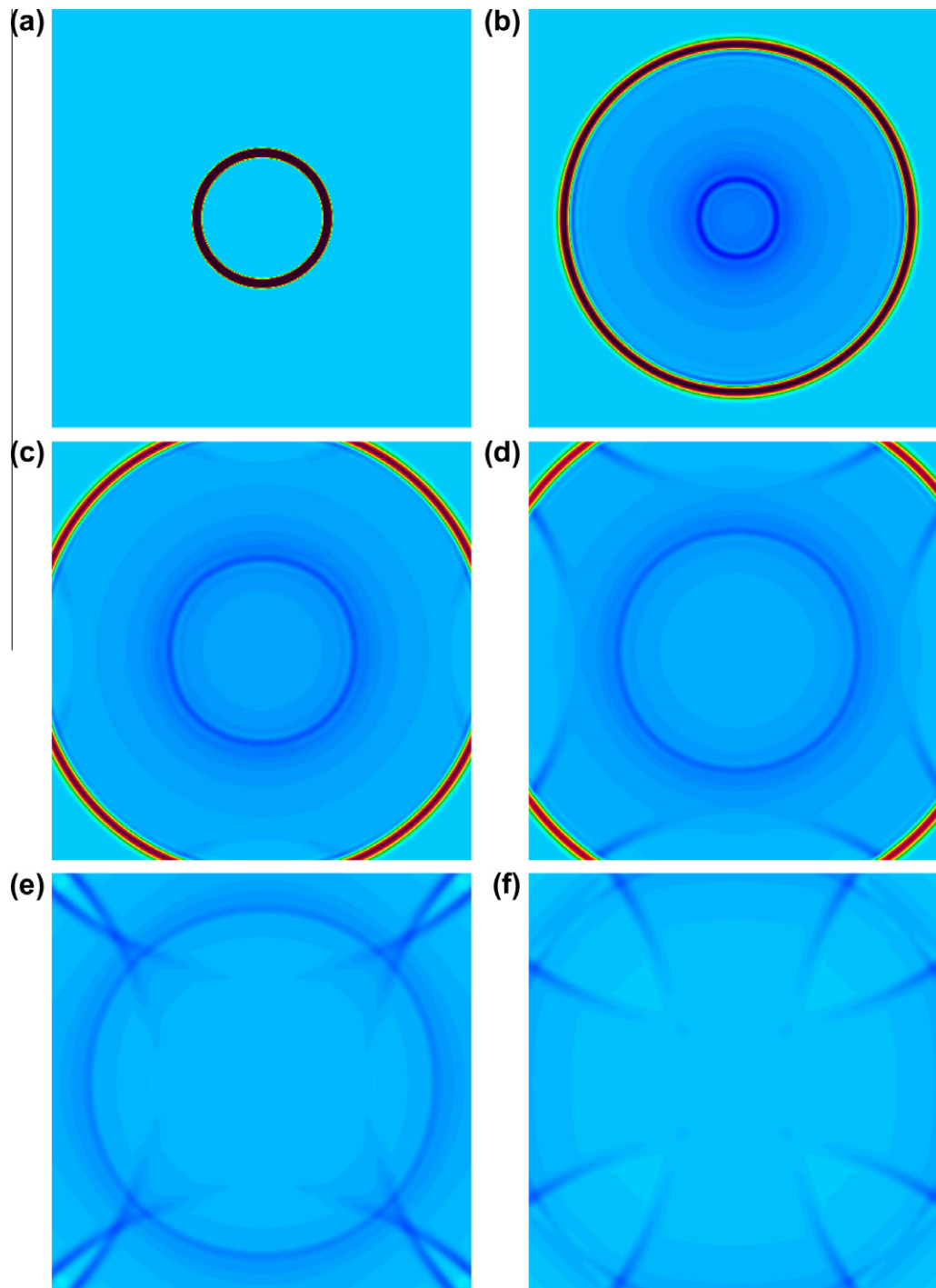
Fig. 3. Wave reflection using the modified Flather open boundary condition. Panels (a)–(f) show the sea surface height signal of a wave radiating outward from the centre. Subsequent panels show a minor reflection with an amplitude of 1% of the outgoing wave back into the domain. No boundary trapped phenomena are present.

the domains. θ is a refinement parameter that determines the magnitude of *stretching* of the vertical grid in either the surface (θ_s) or bottom layers (θ_b). We use no refinement at the bottom ($\theta_b = 0$).hc is a depth above which the vertical grid spacing of the sigma layers becomes (a) nearly uniform and (b) nearly independent of local depth, h, as long as $h \gg hc$. The model bathymetries are taken from (a) the ETOPO2 2-min topography of Smith and Sandwell (1997) for L0 and (b) the GEBCO 1-min topography of Hunter and Macnab (2003) for L1. To prevent aliasing due to undersampling when interpolating to the model grids, the raw topographies are smoothed using a Gaussian filter of width of

twice the model resolution. Since ROMS uses a sigma-coordinate, the topographic steepness must be limited in order to avoid pressure gradient errors. The interpolated topographies are smoothed by selectively applying a local filter to reduce the r-factor to below 0.2 ($r = \triangle h/2h$; e.g., Haidvogel and Beckmann, 1999). All depths shallower than 15 m (5 m) in L0 (L1) are reset to 15 m (5 m). See Section 2.3.1 for more on the preparation of the L1 grid.

The two grids both employ the same climatological forcing at the surface. Wind stress is taken from the QuikSCAT-based Scatterometer Climatology of Ocean Winds (SCOW, Risien and Chelton, 2008). Heat fluxes and precipitation come from the Comprehensive
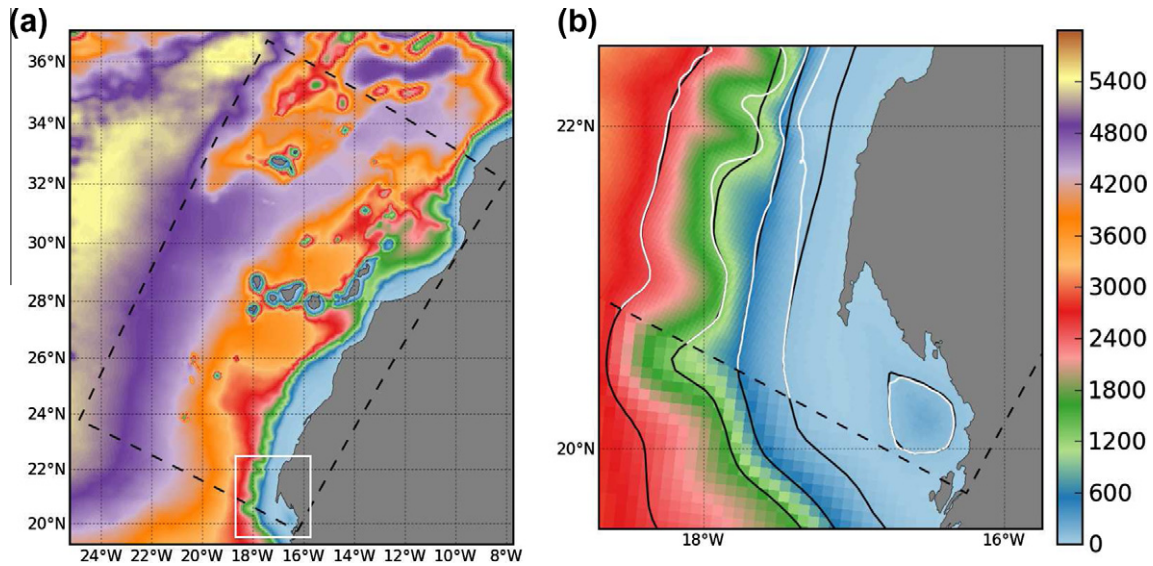
Fig. 4. (a) Child (L1) model domain (dashed black line) and topography of the Canary upwelling region, shown embedded within the parent (L0) domain (shown in Fig. 1). (b) Zoom of the topography over the white box in (a), demonstrating the matching of L1 topography to that of L0 in the boundary region. Child (parent) isobaths are shown in white (black). Isobaths are at 100, 500, 1250 and 2500 m.

Ocean–Atmosphere Dataset (COADS; da Silva et al., 1994; Woodruff et al., 1998), with a mild sea surface temperature (SST; 9-km Pathfinder, Kilpatrick et al., 2001) and sea surface salinity restoring (Barnier et al., 1995). The forcing files are created using the tools described by Penven et al. (2008). The L1 initial and lateral boundary forcing files are prepared following the procedures laid out in Section 2.3. See Mason (2009) for more on the preparation of the L0 initialisation and boundary files.

An L1 Base Case (BC) solution is run for 10 years, with averages of the outputs saved every 2 days. The baroclinic time step is 540 s. At runtime there are two input parameters which influence boundary behaviour: the sponge and the baroclinic normal velocity nudging time scale, $M3$. We apply a weak sponge layer at the boundaries, with the viscosity coefficient, A_h, decaying from $10 \text{ m}^2 \text{ s}^{-1}$ at the boundary to zero at the inner part of the sponge. Such a low value was chosen because we are interested in velocity anomalies at the boundary, which a stronger sponge may smooth away. The eventual use of small sponge values was anticipated by Marchesiello et al. (2001): high-resolution absolute velocities

at the boundaries may minimise differences between parent and evolving child solution to such an extent that the sponge is largely redundant. We set the velocity nudging coefficient $M3 = 0.1$, 10 days for the respective incoming and outgoing flows. These values were chosen considering a typical advective time scale: for our 3-km grid with maximum velocities of $\sim$0.4 m s^{-1}, we obtain 3000/0.4 = 7500 s $\approx$ 0.1 days for the inflow. Given the upwind advection scheme used by ROMS, the outflow parameterisation is less critical than the inflow, and so we set it to 10 days.

2.3. Downscaling methodology

In this section we describe the interpolation of the model prognostic variables from a parent ROMS solution to child boundary and initial files.

2.3.1. Preparation of the child grid
Advance preparation of the child grid, beyond the description given in Section 2.2, is important to facilitate the interpolation. At higher resolutions steep slopes, such as at continental shelf
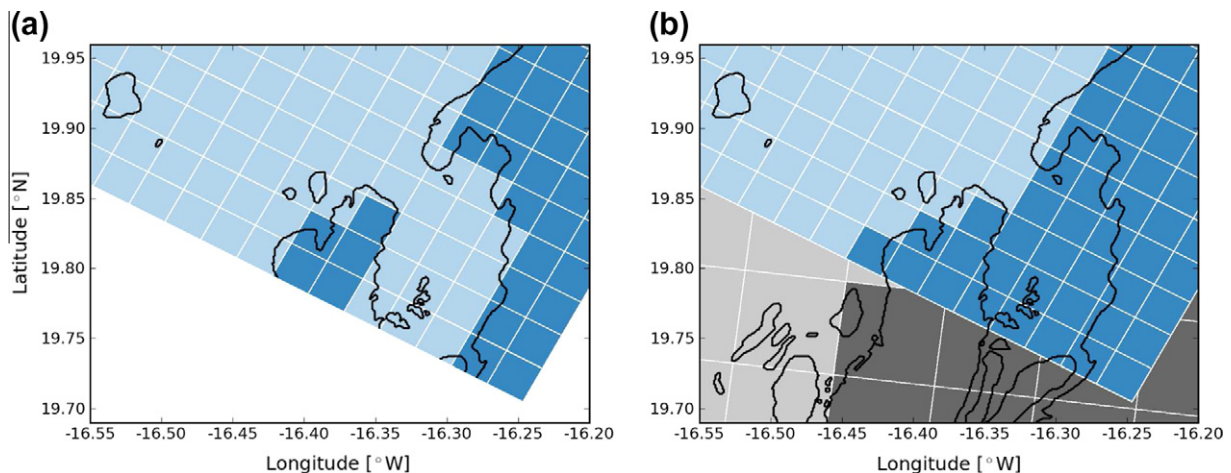

Fig. 5. Schematic diagrams showing the landmasking (darker blue) just north of Cape Timiris on the southeastern corner of the child (L1) domain. In (a) we show a grid where the landmasking is based only on the visible coastline (shown in black), so that an open channel is created. The L1 base case grid is shown in (b); here we include the parent mask (darker grey) to illustrate the need for correspondence between the parent and child masks near their boundary, hence leading to the omission of the open channel. (For interpretation of the references to colour in this figure legend, the reader is referred to the web version of this article.)
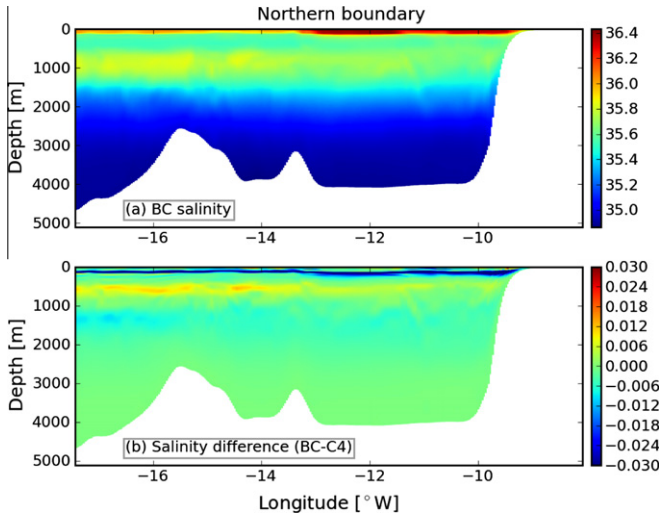
Fig. 6. (a) Salinity section at the northern boundary taken from the BC boundary forcing file at day 800 (year 2 month 6 day 20). (b) The difference between BC salinity in (a) and a transformed salinity section (C4). The transformation involves shifting the salinity values downwards by up to a maximum of 20 m at the depth of the thermocline.

edges, islands, ridges and seamounts, are better resolved than at lower resolutions. This means that depth mismatches between child and parent grids may be significant in these regions and become a problem when they lie along open boundaries, because volume conservation is difficult to enforce. Fig. 4bb illustrates the potential for such a problem. The child isobaths (white) in the interior of the L1 domain are seen to diverge from the parent isobaths (black). In order to prevent such a situation occurring near to the boundaries, topography mismatches are minimised by applying (e.g., Penven et al., 2006):

$$h^{child} = \alpha h^{child} + (1 - \alpha)h^{iparent}, \tag{8}$$

where h^{child} is the child-grid bottom topography, and $h^{iparent}$ is the parent topography interpolated to the child grid. α is a parameter that ranges from 0 at the lateral boundary to 1 over a distance d (typically 10% of the domain) inside the domain.

We also stress that, when defining the child landmask close to the open boundaries, it is important to pay attention to details of the parent landmask. In Fig. 5aa we show hypothetical landmasking at *rho*-points (ROMS uses the Arakawa-C grid; Arakawa, 1966) on the southeastern corner of the child grid. The coastline (in black) may lead us to naively assume Cape Timiris (on the southern boundary at ~16.4°W) to be separated from land by a 9-km open channel, so that we would construct our landmask accordingly. The landmask that we in fact use in our experiments is shown in Fig. 5(b). The parent mask and full coastline are included, revealing the absence of a channel and, furthermore, that the parent is
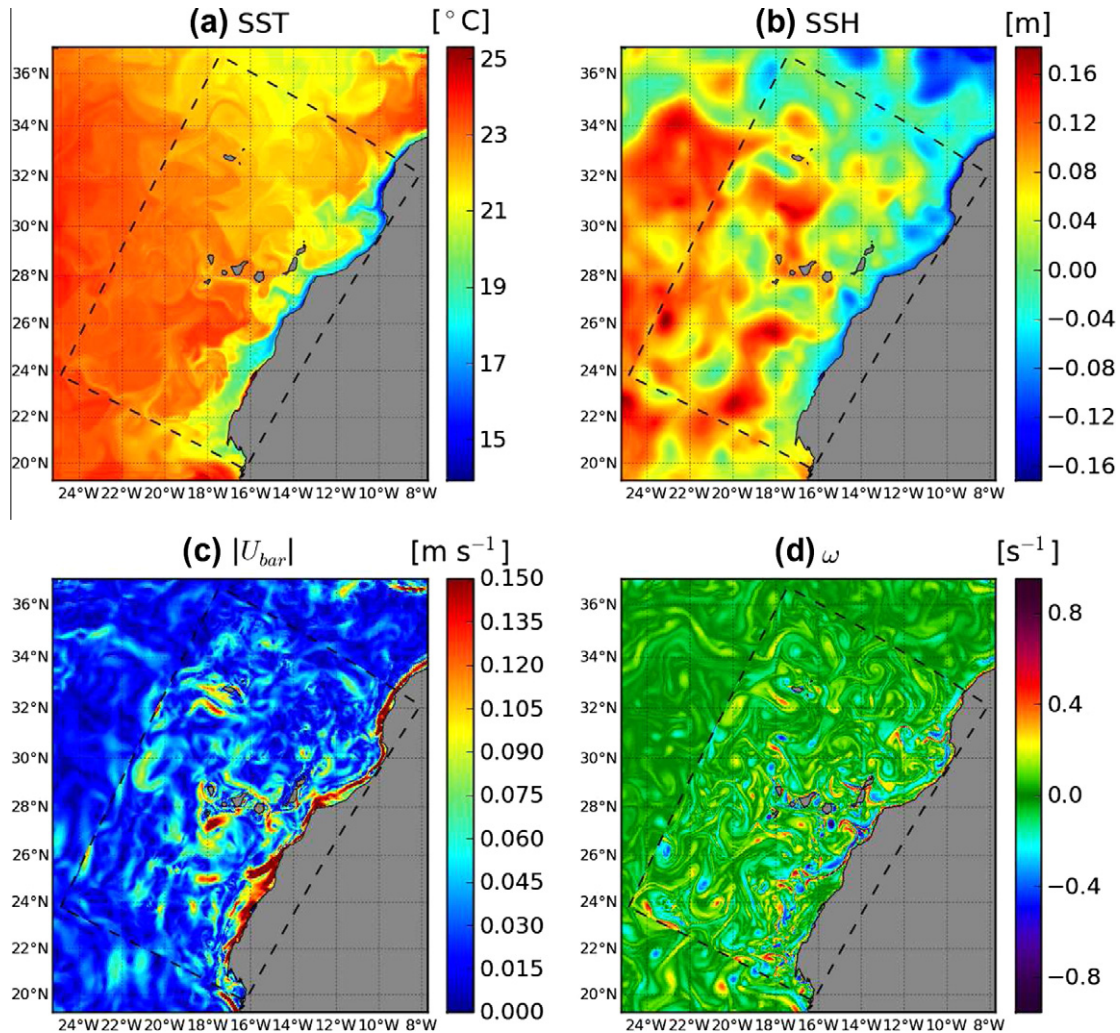

Fig. 7. 2-day child (L1) averages of (a) SST, (b) SSH, (c) barotropic velocity magnitude and (d) surface relative vorticity (ω) in the summer of model year 2, superimposed upon the parent (L0) field which is nearest in time (half a day). Dashed lines mark the L1 boundary.

masked all along the child boundary to as far as one child grid-cell to the west of the cape. We therefore choose to put a corresponding mask into our child grid. This procedure is followed at all open boundaries where landmasking is required.

These steps, that attempt to match child boundaries as closely as possible to those of the parent, work to minimise the need for extrapolation during the interpolation procedure.

2.3.2. Interpolation

The interpolation process is broken down into two stages. For a given time step there is, first, a horizontal stage where the parent variables (both 2D and 3D) are interpolated to the horizontal coordinates (longitude, latitude) of the child domain. In a second, vertical stage for each 3D variable, at each horizontal coordinate in the new matrix, a two-step vertical interpolation transforms the data from parent sigma-coordinates to z-coordinates, and then to child sigma-coordinates. At this point we have the full set of 2D and 3D prognostic variables on the child grid.

To ensure volume conservation, a global barotropic velocity correction is applied to both the baroclinic and barotropic velocities at the open boundaries. The correction, $\overline{U}_{\perp corr}$, is calculated as:

$$\overline{U}_{\perp corr} = - \int_{\Gamma} \overline{U}_{\perp} \cdot h \bigg/ \int_{\Gamma} h, \qquad (9)$$

where $\overline{U}_{\perp}$ is the barotropic normal velocity at the open boundaries, $\int_{\Gamma}$ is a line integral along the open boundaries, and h is the water depth.

Finally, slices are taken from the open boundary sides of each matrix and written to the boundary file. This procedure is applied for each successive time record within a specified time range that is available in the parent solution.

For the present experiments, the L0 solution provides 3-day averages of the prognostic variables. The resulting L1 boundary file contains data at the three open boundaries (north, south, west) of the L1 grid, at the 3-day frequency of L0. As an example, Fig. 6 shows a summer salinity section at the northern boundary. The prominent features are a high salinity surface layer, typical of subtropical eastern North Atlantic Central Water and, centred at about 900 m, a second high salinity layer which corresponds to Mediterranean Water (MW).

2.3.3. Initialisation file extrapolation

An L1 initialisation file containing the full set (2D and 3D) of prognostic variables is built using the first time record extracted from the parent. Here, the essential steps described above are followed. However, in the interior where depth mismatches between parent and child topography do occur, an extrapolation step is sometimes required before the vertical interpolation: If, at a particular point in the respective grids, there is no parent variable at or deeper than the child depth, we search horizontally for the nearest suitable point where the required information is available. This information is then used for the vertical interpolation. This is a relatively simple extrapolation scheme. Recently, Auclair et al. (2006) have demonstrated that crude extrapolation techniques can lead to erroneous currents near steep topography. They propose an optimal scheme to avoid such errors. However, because we use extrapolation only when preparing the initialisation file, our solutions will suffer any such effects only in the very early stages of the model run.

3. Results

In this section we show a series of short-term and long-term averages from our base case (BC) solution of surface fields of SST and the vertical component of the relative vorticity, ω. For the short-term averages we also show Sea Surface Height (SSH), the magnitude of the barotropic velocity, and the mixed layer depth. These demonstrate the quality of the agreement between our L0 and L1 solutions using the methodology described above.

3.1. Instantaneous surface fields

The efficacy of the boundary condition and the boundary preparation procedure is demonstrated in Fig. 7. Two-day averaged (i.e., quasi-instantaneous) surface fields in summer are shown of SST (panel a), SSH (panel b), barotropic velocity (panel c), and ω (normalised by the Coriolis parameter, f) (panel d), are shown. The L1 solution is superimposed upon the temporally-coincident L0 solution (not shown in its entirety). The dashed-line box indicates the boundaries of the L1 grid.

Fig. 7(a) shows a strong upwelling front punctuated by filaments that extend a few hundred kilometers offshore. The most marked of these filaments is that off Cape Ghir at 30.65°N (Pelegrí et al., 2005). Further south, filaments are seen reaching the Canary Islands, where they facilitate exchange of nutrients and organic matter between the African coast and the archipelago (Bécognee et al., 2006; Sandulescu et al., 2006). The eddy-rich wake downstream of the islands peaks in late summer; an anticyclonic eddy is seen just south of the island of Gran Canaria at 28°N. In the offshore region the strongest SST gradients occur along the northern L1 boundary. These are likely related to the Azores front, which is associated with the zonal AzC located at about 34°N (Le Traon and De Mey, 1994). Along the open model boundaries there is little evidence in the SST of discontinuities between the L0 and L1 solutions.

At this point, it is important to repeat the fundamental tenet of a one-way nesting procedure. Since the parent solution is not aware of the child solution, mismatches between child and parent are to be expected, particularly at regions with outflow conditions. This is because the child domain can resolve processes that the parent cannot, leading to eddy fields that can be different. This should not be considered a deficiency of the formulation of the
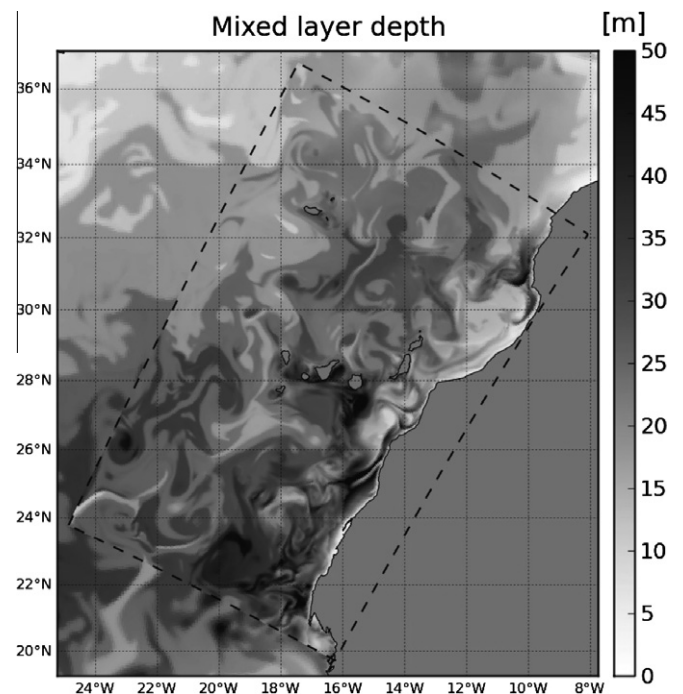

Fig. 8. 2-day child (L1) average of the mixed layer depth in the summer of model year 2, superimposed upon the parent (L0) field which is nearest in time (half a day). Dashed lines mark the L1 boundary.
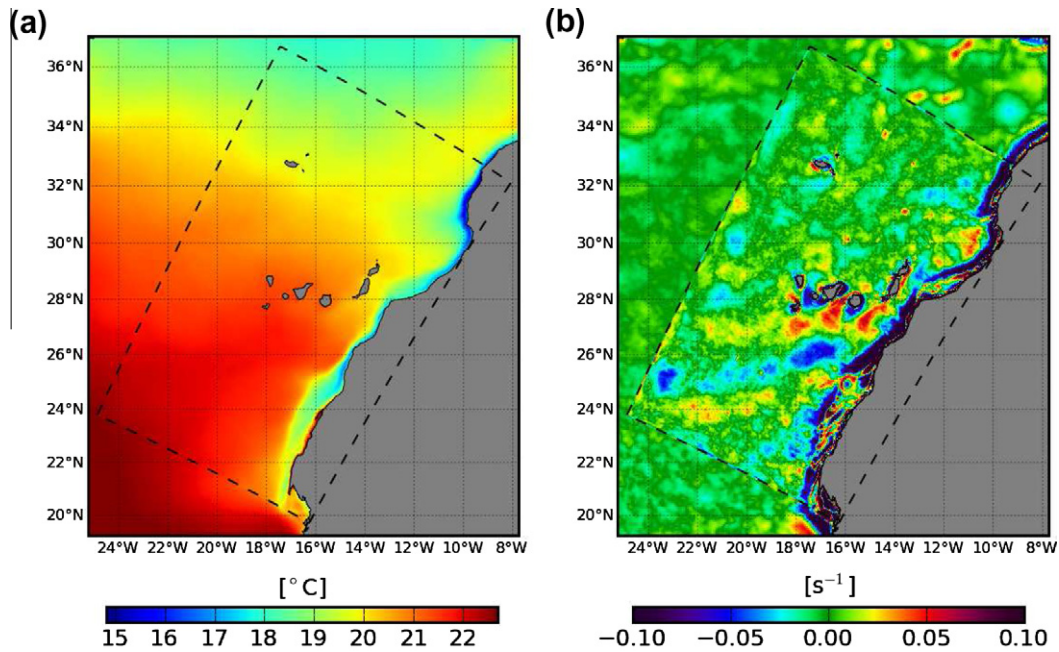
Fig. 9. Child (L1) 7-year annual averages of (a) SST and (b) vorticity (ω) for the base case experiments, superimposed upon the equivalent averages from the parent (L0). Dashed lines show the L1 boundary.
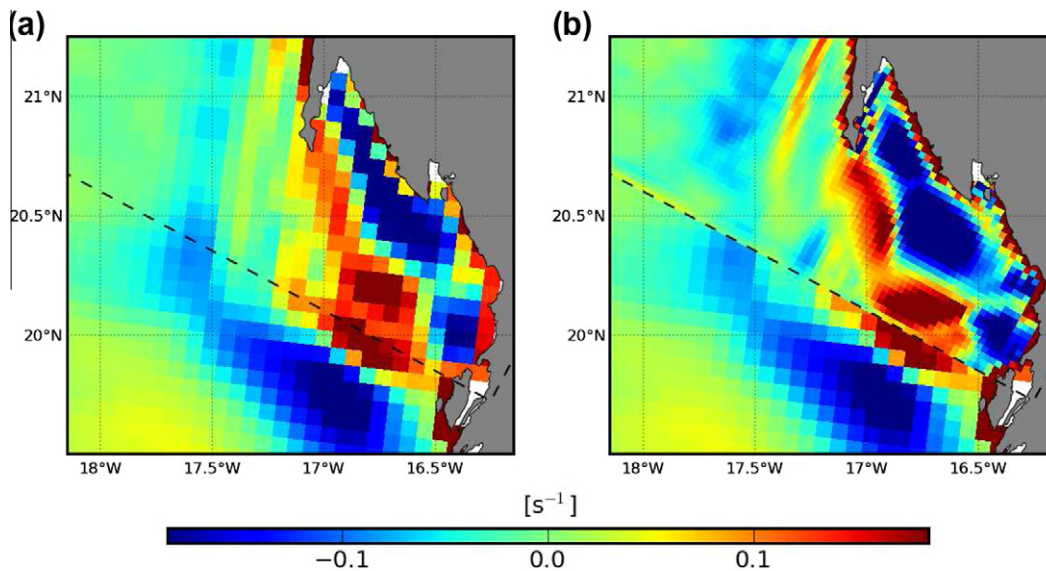

Fig. 10. 7-year annual-mean surface vorticity (ω) at the southeastern corner of the child (L1) domain. In (a) only the parent (L0) ω is shown, while in (b) L1 ω is superimposed upon L0. The dashed black line demarks the L1 boundary. The inshore region shown is the Banc d'Arguin where the water depth is shallow ($\sim$20 m).

Table 1
The sensitivity experiments (C1–C4) in relation to the base case, BC. QC is QuikCOW, the surface wind stress product described in Section 2.2. ds signifies L1 boundary data downscaled from L0.

	Wind stress	Volume conservation	Boundary thermocline
BC	QC	Yes	$(temp, salt)_{ds}$
C1	$QC_u - 0.02$ N m^{-2}	Yes	$(temp, salt)_{ds}$
C2	$QC_v - 0.02$ N m^{-2}	Yes	$(temp, salt)_{ds}$
C3	QC	$(v, \bar{v})_{[N,S]} + 0.5$ cm s^{-1}	$(temp, salt)_{ds}$
C4	QC	Yes	$(temp, salt)_{ds} \Downarrow 20$ m

boundary conditions, but merely a consequence of the one-way nesting approach.

The SSH field in Fig. 7(b) also reveals features related to the coastal upwelling, the island eddy field, and to the AzC. There is very good broad general agreement between the two solutions in the SSH along the length of the L1 boundary. Two mesoscale features in L1 adjacent to the western boundary stand out: at 32.0°N a negative anomaly, and at 26.0°N a positive anomaly. Both structures are examples of features that were either generated within the L1 solution and do not have counterparts in L0 or SSH structures that were intensified in the nested domain thanks to the increased resolution. These anomalies do not show up in the SST of Fig. 7(a). However, in the barotropic velocity of Fig. 7(c) both features are visible near the western L1 boundary.

The sternest test of the boundary behaviour is provided by considering the ω field in Fig. 7(d). L1 ω, owing to the increased grid res-
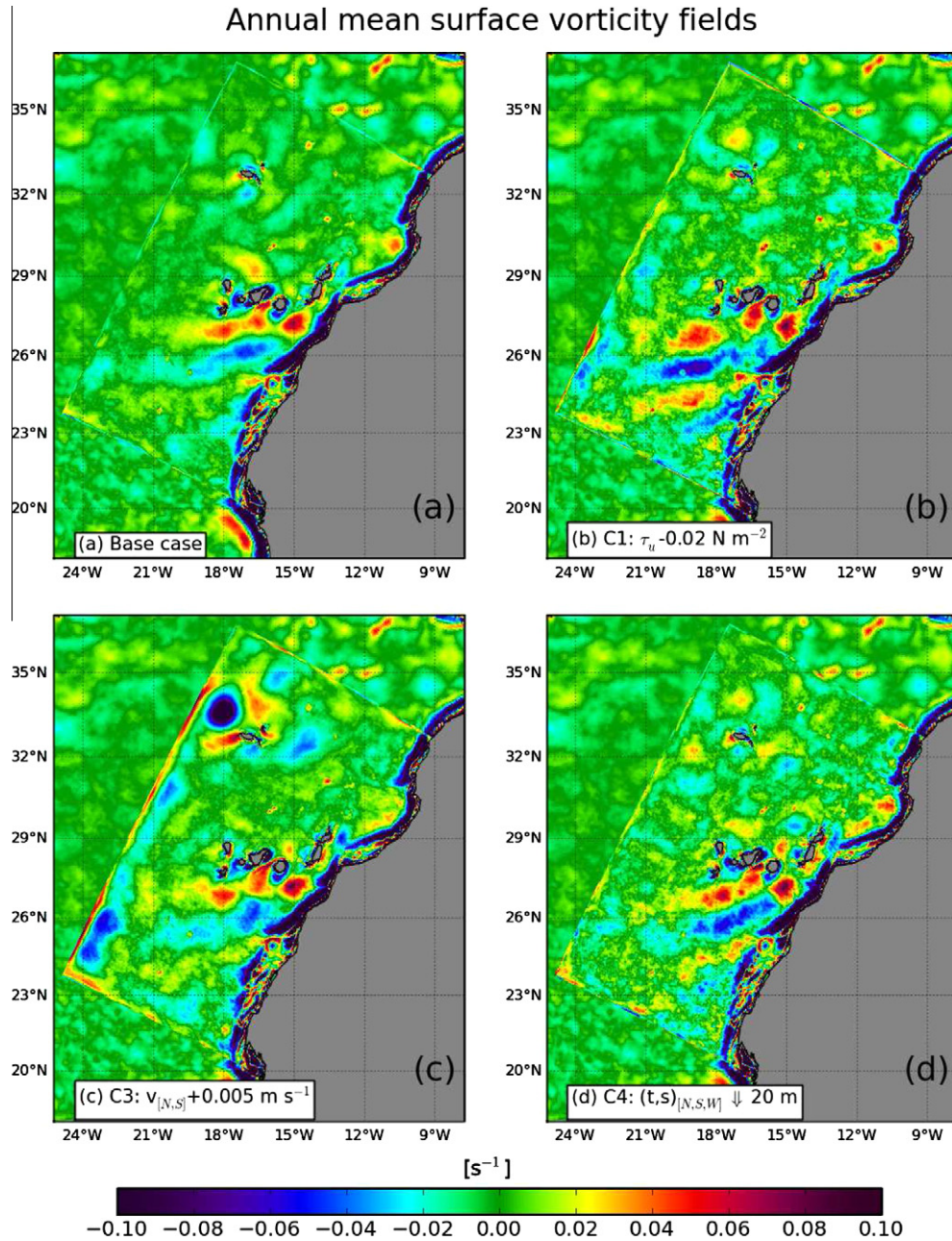
Annual mean surface vorticity fields

Fig. 11. Annual mean surface relative vorticity (ω) fields from (a) the base case experiment, (b) case 1, (c) case 3 and (d) case 4. See Table 1 for a summary of the cases. The L1 boundary is intentionally not demarked.

olution, has a noticeably greater amplitude than that of L0 (also evident in the barotropic velocity). Agreement between the two solutions is very close at the northern (inflow) boundary as expected. The two features on the western boundary identified above are again visible as cyclonic and anticyclonic anomalies. Along the southern boundary too there are now instances of discontinuities, with elevated ω along the L1 boundary. Again this is evidence of processes that are increasingly well resolved by the inner, nested domain.

A further consideration is the behaviour of the mixed layer depth as determined by KPP (the ROMS vertical mixing scheme) shown in Fig. 8. Here, despite broad general agreement between the two solutions, there are clear differences in the southwestern boundary region. A sharp front extends toward the southwestern corner, a feature which is absent in the parent solution.

As mentioned above, it is consistent with expectations that the best agreement between L0 and L1 in both Figs. 7 and 8 occurs at in-

flow regions along the open boundaries. The one-way nesting approach allows for inner and outer solutions that are different at outflowing boundaries since the parent solution is unaware of the child solution. This is particularly true if (sub) mesoscale variability is high, which is the case for our L1 southwestern boundary. Animations produced with time-series of ω, plotted similarly to Fig. 7(d), show that the quality of agreement at the boundaries is persistent.

3.2. Mean surface fields

Fig. 9 shows L1 7-year annual averages at the surface of SST and normalised ω, superimposed upon corresponding L0 mean fields. The SST field in Fig. 9(a) is typical of eastern boundary upwelling regions, with a band of cooler upwelled surface waters along the coast. The coldest SSTs are found in the vicinity of Cape Ghir at 30.65°N. A frontal region associated with the AzC is seen at 34°N.
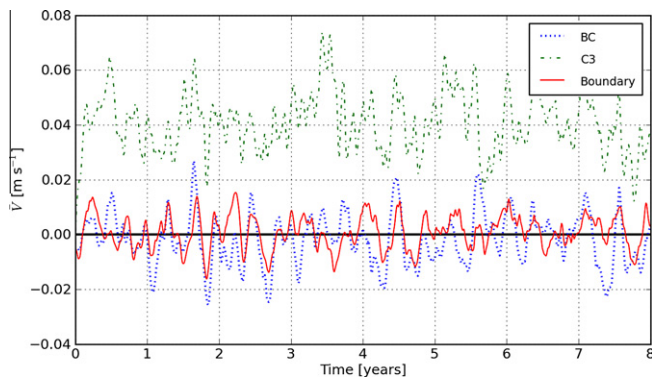
Fig. 12. 8-year time-series of monthly -mean barotropic velocities averaged along the western boundary for BC, C3 and the boundary forcing file. For BC and C3 the average is taken over the three grid point-wide strip along the boundary.

The agreement between L0 and L1 mean SST all along the boundaries is good.

The annual mean surface ω comparison in Fig. 9bb is less clear than the SST. Averaging tends to minimise the signal, so that low values are found in both solutions, particularly in the offshore regions where there is less variability. Along the southern half of the western boundary there is a thin band of trapped cyclonic vorticity, indicative of transient normal velocity mismatching; along the northern half, there is a wider band of anticyclonic activity. To the southwest of the Canary Islands zonal bands of alternating cyclonic and anticyclonic vorticity can be distinguished. These are associated with the Canary Island eddy field (e.g., Sangrà et al., 2009). The most intense band is anticyclonic with a width of ∼1°, centred at ∼25.5°N; its tail at ∼23.5°W appears to have a spuriously high magnitude. Close to the coast, however, there is good agreement between the L0 and L1 vorticity. Trapped against the coast is a strip of intense anticyclonic vorticity, which is bounded by a wider ribbon of cyclonic flow. A closeup of the annual mean coastal ω distribution in the southeast of the domain at the shallow Banc d'Arguin is seen in Fig. 10: (a) shows just the L0 vorticity, (b) shows the L1 vorticity overlain onto L0. The distribution of vorticity is essentially the same in the parent and child solutions. However, the increased resolution of the child domain allows for vorticity structures that are much better resolved.

4. Perturbation experiments

In this section we describe four sensitivity experiments where we attempt to *break* the BC solution described in Section 3. In the first two experiments (C1 and C2) we introduce a small modification to the surface wind forcing. In the third experiment (C3) we perturb the volume conservation imposed by our methodology. In the final experiment (C4) the depth of the thermocline in the boundary files is artificially lowered by up to 20 m. Table 1 provides a summary of the experiments. A comparison between BC and C1, C3 and C4 is given in Fig. 11, which shows annual averages (26 years for BC, 7 years for C1, C3 and C4) of surface ω (normalised by f). The aim of the sensitivity experiments is to explore the robustness of the boundary condition under a variety of credible less-than-perfect forcing scenarios, such as may be encountered when downscaling from an Ocean General Circulation Model (OGCM) to ROMS.

Fig. 11(a) shows the BC surface ω field embedded within that of L0. This is a long-term mean, 26 years, which contains less noise in comparison with the 7-year mean of Fig. 9. The largest vorticity signals are found all along the coast, positive at the coastal bound-

ary and negative just offshore. The Canary Island wake constitutes the other dominant signal, traces of which extend as far as the western boundary at ∼25°N.

4.1. Modified wind experiments (C1,C2)

Two experiments were run where the surface forcing wind stress field was modified with respect to BC. For C1 (C2), 0.02 N m^{-2} was subtracted from the u-component (v-component) of the wind stress for each month of the surface forcing climatology. Fig. 11(b) shows the C1 surface ω. The patterns are generally similar to BC, with largest values associated with the coastal region and the Canary Island wake. The further reaches of the wake (∼19°W), however, have considerably larger ω magnitudes than BC. At the boundaries, there are conspicuous strips of anomalous positive ω, in particular at the western boundary. The C2 surface ω field is not shown as it is not markedly different in character from C1.

4.2. Barotropic flux perturbation experiment (C3)

In this experiment the baroclinic and barotropic normal velocities (v, $\bar{v}$) applied at the northern and southern boundaries are altered by adding a constant value of 0.5 cm s^{-1}, effectively removing the volume conservation imposed during boundary file creation. The effect of this perturbation is clearly seen in the mean surface ω field along the western boundary in Fig. 11(c), in the form of a large anticyclonic standing eddy. The latitudinal position of this eddy, which has a radius of ∼1.5°, is that of the incoming AzC. Along almost the entire western boundary, C3 surface ω is strongly positive, exceeding that of the wind cases. In addition, a wide strip of negative ω runs parallel to the positive boundary anomaly. The overall pattern of ω in the interior is similar to BC.

4.3. Mixed layer depth perturbation experiment (C4)

In the final perturbation experiment, temperature and salinity in the boundary forcing is lowered in depth, by up to a maximum of 20 m in the region of the thermocline. The depth change was done by setting $hc = 80$ (Section 2.2) during the boundary file creation process. Fig. 6(b) illustrates the transformation by showing the difference between a BC and modified C4 salinity section at the northern boundary. The largest differences, positive and negative, correspond to the two high salinity layers seen in Fig. 6(a), the surface and the MW depth layer. Below about 2500 m differences tend to zero. The intention behind this modification is to introduce into the ROMS solution, a small but significant horizontal density gradient within the region of, and normal to, the open boundaries.

The C4 annual mean surface ω is shown in Fig. 11(d). The effect of the thermocline perturbation is most visible along the western boundary, in the form of a narrow intermittent strip of positive vorticity with a similar magnitude to that in C2. In the interior, the far-field island wake vorticity is somewhat greater than it is for BC.

4.4. Discussion

Our choice of perturbations was motivated by the ongoing need to go beyond a ROMS-to-ROMS downscaling (i.e., where the parent is a ROMS solution). We want to be able to downscale at will from model outputs other than ROMS, such as OGCMs like SODA (Carton and Giese, 2008), and also from climatologies. In these situations, all of the above perturbations may come into play: the OGCM is likely to employ a different vertical mixing scheme from ROMS, and to be forced with a different wind stress product. For this reason we chose perturbations (0.02 N m^{-2} and
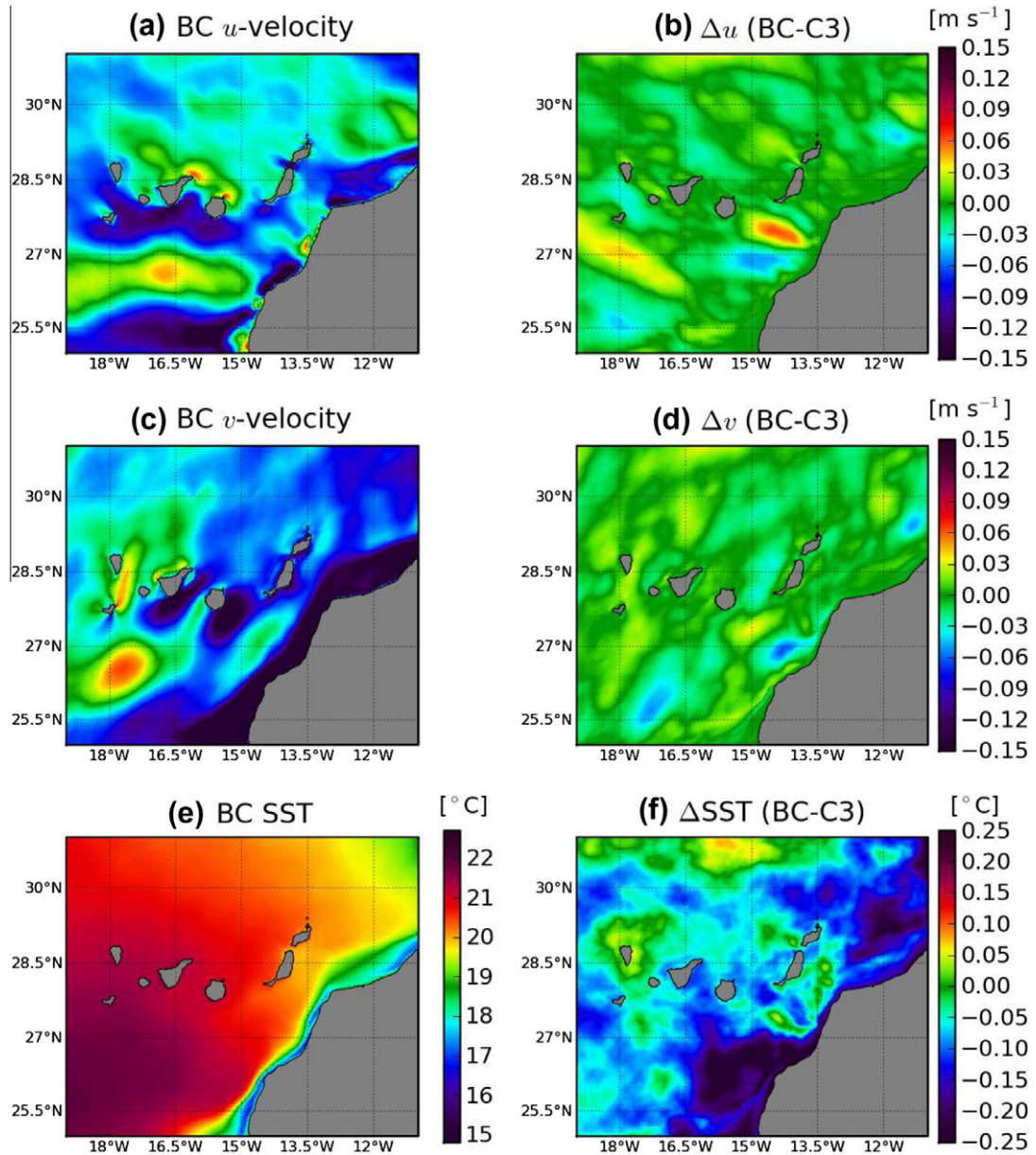
Fig. 13. Zoom near the Canary Islands of long-term annual mean surface fields of *u*-velocity, *v*-velocity and SST for BC (left panel) and their differences from C3 (BC-C3, right panel). The variables are (a,b): *u*, △*u*; (c,d): *v*, △*v*; (e,f): SST, △SST.

20 m, respectively) comparable to the expected differences that may be found between typical OGCM and child ROMS values. We note, however, that our wind perturbations are constants, so that we are not considering wind stress curl differences (between ROMS and OGCM) which may be significant. Our results show that ROMS is relatively robust in response to the perturbations, although the mean solutions presented do show some degradation (Fig. 11(b) and (d)).

Of the perturbations (C1–C4), our methodology is only able to "fix" C3. We show in Fig. 11(c) that, for C3 where the volume conservation is broken, the mean solution is significantly altered. The noise at the western boundary, in particular the standing eddy, is persistent in the instantaneous records (not shown). Fig. 12 compares 8-year time-series from BC and C3 of the monthly mean tangential barotropic velocity ($\bar{v}$) over a three-point-wide strip along the western boundary:

$$\overline{V} = \frac{1}{N_i \times N_j} \sum_{i=1}^{N_i} \sum_{j=1}^{N_j} \bar{v}_{ij}, \tag{10}$$

where $N_i = 3$ and $N_j = 534$. $\overline{V}$ is also computed from the boundary forcing file with $N_i = 1$. The figure shows that the effect of perturbation C3 is rapid: within a couple of months from the initialisation, C3 $\overline{V}$ is strongly positive and does not approach zero thereafter, indicative of a significant anomaly at the boundary (i.e., rim current). BC $\overline{V}$, however, oscillates around the zero mark, as does the boundary $\overline{V}$. The amplitude ranges for both cases are similar, that for the boundary is slightly smaller. Plots for C1, C2 and C4, not shown, lie roughly within the same range as BC.

A further finding of these experiments answers the question: does the quality of the boundary data matter? Modellers place boundaries far away from a region of interest in an attempt to min-

imise the effects of small boundary artifacts on the interior. Fig. 13 shows comparisons of 7-year annual means from BC and C3 of surface fields in the vicinity of the Canary Islands, the centre of the L1 domain. Fig. 13(a), c, e show, respectively, u- and v-velocity components and SST from BC. Differences in these variables between BC and C3 are shown in Fig. 13(b), (d) and (f). The figures show that velocity differences frequently exceed 0.05 m s^{-1} for both u and v, despite the distance from the boundary. Similarly for SST, the ΔSST field shows that BC SST offshore of the shelf edge is cooler than C3 by more than 0.25 °C. These differences strongly suggest that remote forcing does have a global impact upon the model solution, such that the steps taken in our methodology (Section 2.3) are justified.

5. Conclusions

A new formulation of the barotropic open boundary condition is proposed that minimises wave reflection at the open boundaries of the regional domain. High quality ROMS solutions with minimal artifacts at the boundaries are achievable using one-way ROMS-to-ROMS offline nesting techniques, provided that suitable care is taken in the boundary file creation process. The main components of our boundary forcing methodology are accurate interpolation to child grid-points of parent data, matching of the parent–child topography and landmask, and a normal velocity correction at the child boundaries to ensure volume conservation (Section 2.3). The methodology is robust when downscaling to grids with differing vertical resolutions (Mason, 2009).

A major advantage of a boundary forcing that is strictly two-dimensional as opposed to a three-dimensional nudging region is the ability to provide high-frequency boundary information for the inner grid over an extended period of time. This allows the inner grid to be forced with an outer solution that contains meso- or even submesoscale variance in the tracer and velocity fields. Such a nesting strategy provides a unique and convenient approach to study phenomena such as frontal instabilities and submesoscale eddies (Capet et al., 2008a) in a realistic environment in the higher-resolution inner grid (Capet et al., 2008b; McWilliams et al., 2009). When averaging the outer solution to, for instance, monthly means (Dong et al., 2009) one removes the mesoscale variability at the boundaries that is essential for the submesoscale variability to be generated correctly. When a computational domain is large enough, some of the mesoscale variability may be recovered by means of baroclinic instability within the domain. When one is nesting in multiple steps to increasingly higher-resolution domains (but also smaller in physical size), it is essential to retain all of the variability from the parent grid solutions.

A limitation of the current paper is that we still have an incomplete understanding of which properties of the parent solutions are essential to transfer accurately to the child grid. To further our understanding we performed a number of perturbation experiments. From those experiments it appears that the consideration of volume conservation across the open boundaries of the child grid is important. A small correction to the velocities at the boundaries leads to significant tangential velocities at the domain boundaries (Fig. 11). Other types of perturbations lead to responses in the solution of the inner grid that are less pronounced. However, our experience with similar experiments for different parent–child configurations are somewhat inconclusive. What this means is that we are currently able to obtain high-quality solutions when downscaling a ROMS solution to a ROMS configuration. Our ability to downscale arbitrary data such as observations or solutions computed by different models is currently not as advanced. In these latter cases, our methodology is not as capable as evidenced by our parent (L0) solution (see the rim currents in Fig. 1) which was forced with a monthly observation-based climatology.

Finally, we show that small changes in boundary forcing data may lead to differences in the solution throughout the numerical domain (see Fig. 13). Even in cases where the region of interest is located away from the boundaries of the computational domain it remains therefore important to downscale the parent solution properly.

References

Arakawa, A., 1966. Computational design for long-term numerical integration of the equations of fluid motion: two-dimensional incompressible flow. Part I. J. Comput. Phys. 1 (1), 119–143.

Arístegui, J., Sangrà, P., Hernández-León, S., Cantón, M., Hernández-Guerra, A., Kerling, J.L., 1994. Island-induced eddies in the Canary Islands. Deep-Sea Res. 49 (10), 1087–1101.

Auclair, F., Estournel, C., Marsaleix, P., Pairaud, I., 2006. On coastal ocean embedded modeling. Geophys. Res. Lett. 33, L14602.

Barnier, B., Siefridt, L., Marchesiello, P., 1995. Thermal forcing for a global ocean circulation model using a three-year climatology of ECMWF analyses. J. Mar. Sys. 6 (4), 363–380.

Barnier, B., Marchesiello, P., de Miranda, A.P., Molines, J.-M., Coulibaly, M., 1998. A sigma-coordinate primitive equation model for studying the circulation in the South Atlantic. Part I: Model configuration with error estimates. Deep-Sea Res. 45 (4–5), 543–572.

Beckers, J.M., Brasseur, P., Nihoul, J.C.J., 1997. Circulation of the western Mediterranean: from global to regional scales. Deep-Sea Res. 44 (3–4), 531–549.

Bécognee, P., Almeida, C., Barrera, A., Hernández-Guerra, A., Hernández-León, S., 2006. Annual cycle of clupeiform larvae around Gran Canaria Island, Canary Islands. Fish. Oceanogr. 15 (4), 293–300.

Blayo, E., Debreu, L., 2005. Revisiting open boundary conditions from the point of view of characteristic variables. Ocean Modell. 9 (3), 234–252.

Cailleau, S., Fedorenko, V., Barnier, B., Blayo, E., Debreu, L., 2008. Comparison of different numerical methods used to handle the open boundary of a regional ocean circulation model of the Bay of Biscay. Ocean Modell. 25 (1–2), 1–16.

Capet, X.J., Campos, E.J., Paiva, A.M., 2008a. Submesoscale activity over the Argentinian shelf. Geophys. Res. Lett. 35, L15605.

Capet, X.J., McWilliams, J.C., Molemaker, M.J., Shchepetkin, A.F., 2008b. Mesoscale to submesoscale transition in the California current system. Part I: Flow structure, eddy flux, and observational tests. J. Phys. Oceanogr. 38 (1), 29–43.

Carton, J.A., Giese, B.S., 2008. A reanalysis of ocean climate using simple ocean data assimilation (SODA). Mon. Weather Rev. 136 (8), 2999–3017.

Chapman, D.C., 1985. Numerical treatment of cross-shelf open boundaries in a barotropic coastal ocean model. J. Phys. Oceanogr. 15 (8), 1060–1075.

Charney, J., Fjortoft, F., VonNeumann, R., 1950. Numerical integration of the barotropic vorticity equation. Tellus 2 (5), 237–254.

da Silva, A.M., Young, C.C., Levitus, S., 1994. Atlas of Surface Marine Data 1994, vols. 1–5. NOAA Atlas NESDIS 6–10, US Government Printing Office.

Debreu, L., 2008. ROMS-AGRIF two-way nesting algorithms: Latest developments. ROMS/TOMS European workshop. 6–8 October, Grenoble, France.

Debreu, L., Blayo, E., 2008. Two-way embedding algorithms: a review. Ocean Dynam., 415–428. Special Issue on Multi-Scale Modelling: Nested Grid and Unstructured Mesh Approaches.

Debreu, L., Vouland, C., Blayo, E., 2008. AGRIF: adaptive grid refinement in Fortran. Comput. Geosci. 34 (1), 8–13.

de Miranda, A.P., Barnier, B., Dewar, W.K., 1999. Mode waters and subduction rates in a high-resolution South Atlantic simulation. J. Mar. Res. 57 (32), 213–244.

Dong, C., Idica, E.Y., McWilliams, J.C., 2009. Circulation and multiple-scale variability in the Southern California bight. Prog. Oceanogr. 82 (3), 168–190.

Estournel, C., Auclair, F., Lux, M., Nguyen, C., Marsaleix, P., 2009. Scale oriented embedded modeling of the north–western Mediterranean in the frame of MFSTEP. Ocean Sci. 5, 73–90.

Flather, R.A., 1976. A tidal model of the north–west European continental shelf. Memoires de la Societe Royale des Sciences de Liège 6 (10), 141–164.

Haidvogel, D.B., Beckmann, A., 1999. Numerical Ocean Circulation Modeling. Imperial College Press.

Hernández-Guerra, A., Fraile-Nuez, E., López-Laatzen, F., Martínez, A., Parrilla, G., Vélez-Belchí, P., 2005. Canary current and north equatorial current from an inverse box model. J. Geophys. Res. 110, C12019.

Hunter, P., Macnab, R., 2003. The GEBCO Digital Atlas published by the British Oceanographic Data Centre on behalf of IOC and IHO. North Atlantic Region.

Kilpatrick, K., Podesta, G.P., Evans, R., 2001. Overview of the NOAA/NASA advanced very high resolution radiometer pathfinder algorithm for sea surface temperature and associated matchup database. J. Geophys. Res. 106 (C5), 9179–9197.

Lam, F.-P.A., Haley Jr., P.J., Janmaat, J., Lermusiaux, P.F.J., Leslie, W.G., Schouten, M.W., te Raa, L.A., Rixen, M., 2009. At-sea real-time coupled four-dimensional oceanographic and acoustic forecasts during battlespace preparation 2007. J. Mar. Sys. 78 (Suppl. 1), S306–S320.

Leslie, W.G., Robinson, A.R., Haley Jr., P.J., Logutov, O., Moreno, P.A., Lermusiaux, P.F.J., Coelho, E., 2008. Verification and training of real-time forecasting of multi-scale ocean dynamics for maritime rapid environmental assessment. J. Mar. Sys. 69 (1–2), 3–16.

Le Traon, P.-Y., De Mey, P., 1994. The eddy field associated with the Azores Front east of the Mid-Atlantic ridge as observed by the Geosat altimeter. J. Geophys. Res. 99 (C5), 9907–9924.

Machín, F., Hernández-Guerra, A., Pelegrí, J.L., 2006. Mass fluxes in the Canary Basin. Prog. Oceanogr. 70 (2–4), 416–447.

Madec, G., 2008. NEMO Ocean Engine (Note du Pole de Modélisation). Technical Report 27, Institute Pierre-Simon Laplace (IPSL), France. ISSN 1288-1619.

Marchesiello, P., Barnier, B., de Miranda, A.P., 1998. A sigma-coordinate primitive equation model for studying the circulation in the South Atlantic. Part II: Meridional transports and seasonal variability. Deep-Sea Res. 45 (4–5), 573–608.

Marchesiello, P., McWilliams, J.C., Shchepetkin, A., 2001. Open boundary conditions for long-term integration of regional oceanic models. Ocean Modell. 3 (1–2), 1–20.

Mason, E., 2009. High-Resolution Modelling of the Canary Basin Oceanic Circulation. Ph.D. Thesis, Universidad de Las Palmas de Gran Canaria, p. 235.

McWilliams, J.C., Colas, F., Molemaker, M.J., 2009. Cold filamentary intensification and oceanic surface convergence lines. Geophys. Res. Lett. 36 (18), L18602.

Onken, R., Robinson, A.R., Kantha, L., Lozano, C.J., Haley, P.J., Carniel, S., 2005. A rapid response nowcast/forecast system using multiply nested ocean models and distributed data systems. J. Mar. Sys. 56 (1–2), 45–66.

Orlanski, I., 1976. A simple boundary condition for unbounded hyperbolic flows. J. Comput. Phys. 21, 251–269.

Pelegrí, J.L., Marrero-Díaz, A., Ratsimandresy, A., Antoranz, A., Cisneros-Aguirre, J., Gordo, C., Grisolía, D., Hernández-Guerra, A., Láiz, I., Martínez, A., Parrilla, G., Pérez-Rodríguez, P., Rodríguez-Santana, A., Sangrà, P., 2005. Hydrographic cruises off northwest Africa: The Canary current and the Cape Ghir region. J. Mar. Sys. 54 (1–4), 39–63.

Penven, P., Debreu, L., Marchesiello, P., McWilliams, J.C., 2006. Evaluation and application of the ROMS 1-way embedding procedure to the central California upwelling system. Ocean Modell. 12 (1–2), 157–187.

Penven, P., Marchesiello, P., Debreu, L., Lefevre, J., 2008. Software tools for pre- and post-processing of oceanic regional simulations. Environ. Model. Softw. 23, 660–662.

Perkins, A.L., Smedstad, L.F., Blake, D.W., Heburn, G.W., Wallcraft, A.J., 1997. A new nested boundary condition for a primitive equation ocean model. J. Geophys. Res. 102 (C2), 3483–3500.

Risien, C.M., Chelton, D.B., 2008. A global climatology of surface wind and wind stress fields from eight years of QuikSCAT scatterometer data. J. Phys. Oceanogr. 38 (11), 2379–2413.

Robinson, A.R., 1999. Forecasting and simulating coastal ocean processes and variability with the harvard ocean prediction system. In: Coastal Ocean Prediction. Coastal and Estuarine Studies Series. American Geophysical Union, pp. 77–100.

Sandulescu, M., Hernández-Garcia, E., López, C., Feudel, U., 2006. Kinematic studies of transport across an island wake, with application to the Canary islands. Tellus 58 (5), 605–615.

Sangrà, P., Pelegrí, J.L., Hernández-Guerra, A., Arregui, I., Martín, J.M., Marrero-Díaz, A., Martínez, A., Ratsimandresy, A.W., Rodríguez-Santana, A., 2005. Life history of an anti-cyclonic eddy. J. Geophys. Res. 110, C03021.

Sangrà, P., Pascual, A., Rodríguez-Santana, Á., Machín, F., Mason, E., McWilliams, J.C., Pelegrí, J.L., Dong, C., Rubio, A., Arístegui, J., Marrero-Díaz, Á., Hernández-Guerra, A., Martínez-Marrero, A., Auladell, M., 2009. The Canary Eddy Corridor: a major pathway for long-lived eddies in the subtropical North Atlantic. Deep-Sea Res. 56, 2100–2114.

Shchepetkin, A.F., McWilliams, J.C., 2005. The regional oceanic modeling system (ROMS): a split-explicit, free-surface, topography-following-coordinate oceanic model. Ocean Modell. 9 (4), 347–404.

Shchepetkin, A.F., McWilliams, J.C., 2009. Correction and commentary for "Ocean forecasting in terrain-following coordinates: formulation and skill assessment of the regional ocean modeling system" by Haidvogel et al., J. Comput. Phys. 227, pp. 3595–3624. J. Comput. Phys. 228, 8985–9000.

Smith, W.H.F., Sandwell, D.T., 1997. Global sea floor topography from satellite altimetry and ship depth soundings. Science 277 (5334), 1956–1962.

Tejera, A., García-Weil, L., Heywood, K., Cantón-Garbín, M., 2002. Observations of oceanic mesoscale features and variability in the Canary Islands area from ERS-1 altimeter data, satellite infrared imagery and hydrographic measurements. Int. J. Remote Sens. 23 (22), 4897–4916.

Woodruff, S.D., Diaz, H.F., Elms, J.D., Worley, S.J., 1998. COADS release 2 data and metadata enhancements for improvements of marine surface flux fields. Phys. Chem. Earth 23 (5), 517–526.